
Hyper-Connections for Adaptive Multi-Modal MRI Brain Tumor Segmentation

Lokendra Kumar

lokendra63@alumni.iitm.ac.in

Shubham Aggarwal

Shubham_agg@alumni.iitm.ac.in

Abstract

We present the first study of Hyper-Connections (HC) for volumetric multi-modal brain tumor segmentation, integrating them as a drop-in replacement for fixed residual connections across five architectures: nnU-Net, SwinUNETR, VT-UNet, U-Net, and U-Netpp. Dynamic HC consistently improves all 3D models on the BraTS 2021 dataset, yielding up to +1.03% mean Dice gain with negligible parameter overhead. Gains are most pronounced in the Enhancing Tumor sub-region, reflecting improved fine-grained boundary delineation. Modality ablation further reveals that HC-equipped models develop sharper sensitivity toward clinically dominant sequences, specifically T1ce for Tumor Core and Enhancing Tumor, and FLAIR for Whole Tumor, a behavior absent in fixed-connection baselines and consistent across all architectures. In 2D settings, improvements are smaller and configuration-sensitive, suggesting that volumetric spatial context amplifies the benefit of adaptive aggregation. These results establish HC as a simple, efficient, and broadly applicable mechanism for multi-modal feature fusion in medical image segmentation.

1 Introduction

Brain tumors are among the most life-threatening neurological disorders, requiring precise diagnosis and treatment planning to improve patient survival and quality of life. Magnetic Resonance Imaging (MRI) is widely used for brain tumor assessment due to its ability to capture detailed soft tissue structures. However, manual delineation of tumor regions is time-consuming, subjective, and prone to inter-observer variability. Automated segmentation models have therefore become essential in modern clinical workflows, enabling accurate identification of tumor sub-regions such as Enhancing Tumor (ET), Tumor Core (TC), and Whole Tumor (WT). Reliable segmentation directly impacts downstream tasks including surgical planning, radiotherapy targeting, disease progression monitoring, and treatment response evaluation, making it a critical component in medical image analysis.

The BraTS benchmark [11, 2] has standardized multi-modal brain tumor segmentation using four MRI sequences T1, T1ce, T2, and FLAIR, which provide complementary information about tumor structure and pathology. Over the years, a wide range of architectures have been developed for this task. For volumetric (3D) segmentation, models such as nnU-Net [8], SwinUNETR [3], and VT-UNet [13] have demonstrated strong performance by capturing spatial context and global dependencies. For slice-wise (2D) segmentation, architectures including U-Net [14] and U-Netpp [17] remain widely used due to their efficiency and effectiveness. Despite these differences, most approaches rely on fixed residual and skip connections for feature aggregation, which are inherently input-independent and limit the model’s ability to adapt to varying modality importance and tumor characteristics.

In this work, we explore Hyper-Connections (HC) [18], a recently proposed generalization of residual connections that enables dynamic, input-dependent feature aggregation. While HC has shown promising results in domains such as large language models and image generation and classification, it has not been investigated for medical image segmentation, particularly in volumetric and multi-modal settings. We extend HC to both 3D and 2D segmentation architectures and systematically

evaluate its integration across nnU-Net, SwinUNETR, VT-UNet, U-Net, and U-Netpp. Our work demonstrates the effectiveness of HC in improving segmentation performance and provides insights into modality importance, showing how adaptive connections enable better utilization of multi-modal MRI information.

2 Related Work

Brain tumor segmentation has been extensively studied through the BraTS challenge [11, 2], with U-Net [14] establishing the encoder-decoder paradigm with skip connections as a dominant approach. nnU-Net [8] further advanced this direction by automating preprocessing, architecture configuration, and training strategies, and remains a strong convolutional baseline. Transformer-based approaches have introduced improved global context modeling, including UNETR [4], which employs a transformer encoder with a convolutional decoder, SwinUNETR [3], which leverages hierarchical shifted-window attention [9], and VT-UNet [13], which incorporates volumetric self-attention with 3D positional encoding. Despite these advances, all such architectures rely on fixed and non-adaptive connection mechanisms.

Adaptive connection and attention mechanisms have been explored to improve feature representation and training dynamics. Residual connections [5] enable stable optimization of deep networks through identity mappings, while Squeeze-and-Excitation networks [7] introduce channel-wise adaptive reweighting. Attention gates [12] enhance skip connections by focusing on relevant spatial regions. Other approaches such as ReZero [1] and ResiDual [15] modify residual pathways to improve convergence and stability. However, these methods typically target specific connection types or architectural components. In contrast, the Hyper-Connection framework [18] provides a unified formulation that simultaneously adapts both depth-wise and width-wise connections, representing a strict generalization of prior approaches. To the best of our knowledge, this work presents the first evaluation of hyper-connections in volumetric medical image segmentation.

Multi-modal and multi-scale feature fusion is central to MRI-based segmentation. U-Netpp [17] introduced densely nested skip connections to bridge the semantic gap between encoder and decoder representations, while attention-based methods [12] learn to emphasize spatially relevant features. Prior work has also explored modality-specific weighting strategies for BraTS segmentation [16]. Hyper-connections generalize these ideas by enabling adaptive aggregation across all connections in the network, conditioned on global input statistics at each layer, thereby providing a unified and flexible mechanism for multi-modal feature integration.

3 Background and Motivation

3.1 From Language Models to Volumetric Medical Imaging

Hyper-Connections (HC) were originally proposed in the context of large language model pre-training, where the primary challenge is to maintain stable gradient flow across very deep transformer architectures operating on sequential token embeddings [18]. In that setting, HC improves optimization by learning adaptive depth-wise aggregation, thereby avoiding limitations associated with fixed residual formulations such as Pre-Norm and Post-Norm variants. In contrast, volumetric medical image segmentation presents a fundamentally different problem. Instead of discrete tokens, the input consists of continuous-valued three-dimensional voxel grids, and the output requires dense, voxel-level predictions with high spatial precision. Furthermore, MRI-based segmentation is inherently multi-modal, with sequences such as T1, T1ce, T2, and FLAIR providing complementary but unevenly informative signals. The task is further complicated by the nested anatomical structure of tumor sub-regions and the reliance on encoder-decoder architectures with skip connections that preserve spatial correspondence. These differences raise an important question: whether the benefits of HC extend beyond sequence modeling to structured, multi-modal, and spatially grounded tasks such as medical image segmentation.

3.2 Limitations of Fixed Connections in Multi-Modal MRI Segmentation

Most existing architectures rely on fixed residual connections of the form

$$x_{l+1} = x_l + F(x_l), \tag{1}$$

where the contribution of the residual branch is constant and independent of the input [5]. Similarly, skip connections in encoder-decoder architectures combine features using fixed rules such as concatenation or summation. While effective in general settings, such fixed aggregation introduces several limitations in multi-modal MRI segmentation. First, these connections are modality-blind, meaning they cannot dynamically adjust the contribution of different MRI sequences, even though modalities such as FLAIR and T1ce capture distinct biological characteristics. Second, they impose depth-invariant weighting, treating shallow and deep features equally across all spatial regions, despite the fact that different tumor sub-regions require different levels of semantic and textual information. Third, they do not account for the hierarchical structure of tumor regions, where Enhancing Tumor is contained within Tumor Core, which is further contained within Whole Tumor. Finally, fixed connections are inherently patient-invariant, applying the same aggregation strategy to all inputs, even though tumor appearance varies significantly across patients. These limitations motivate the need for adaptive connection mechanisms that can adjust feature aggregation based on input characteristics.

3.3 Adaptive Multi-Modal Feature Aggregation in HC-Powered Architectures

Multi-modal input formalisation. Let the BraTS input for a single subject be $\mathbf{X} = [X^{(1)}, X^{(2)}, X^{(3)}, X^{(4)}]$, where $X^{(m)} \in \mathbb{R}^{H \times W \times D}$ for $m \in \mathcal{M} = \{\text{T1}, \text{T1ce}, \text{T2}, \text{FLAIR}\}$. After a shared initial projection ϕ , the fused representation entering the backbone is $x_0 = \phi(\mathbf{X}) \in \mathbb{R}^{B \times C \times L}$, where $L = H \times W \times D$ denotes the number of spatial tokens and C the feature dimension.

Modality sensitivity under residual connections. In a standard residual network, as described in [6], the feature at layer l is updated as

$$x_{l+1}^{\text{res}} = x_l^{\text{res}} + F_\theta(x_l^{\text{res}}), \quad x_0^{\text{res}} = x_0. \quad (2)$$

The sensitivity of the final representation to modality m , measured via the Jacobian, is

$$\frac{\partial x_L^{\text{res}}}{\partial X^{(m)}} = \frac{\partial x_0}{\partial X^{(m)}} \prod_{l=0}^{L-1} (I + J_{F_\theta}(x_l^{\text{res}})), \quad (3)$$

where J_{F_θ} denotes the Jacobian of F_θ . The factor $\frac{\partial x_0}{\partial X^{(m)}}$ is determined entirely by the input projection ϕ and is constant across layers, patients, and spatial locations. Modality influence is therefore mediated indirectly through the accumulated nonlinear path $\prod_l (I + J_{F_\theta})$, with no explicit mechanism for re-weighting modalities according to tumour sub-region or patient-specific appearance. Any modality selectivity that emerges in such architectures is purely a product of the data distribution learned through F_θ , without architectural support for spatially or contextually varying aggregation. (This formulation is illustrative; in practice, Jacobian accumulation across L layers can be numerically unstable.)

Modality sensitivity under Hyper-Connections. HC replaces the scalar residual with a learned aggregation over n parallel feature streams. The hyper-hidden state is initialised as

$$H_0 = x_0 \otimes \mathbf{1}_n^\top \in \mathbb{R}^{B \times L \times n \times C}, \quad (4)$$

producing n identically initialised copies that subsequently evolve through distinct mixing trajectories. The Static HC (SHC) update is

$$H_{l+1}^{\text{SHC}} = \underbrace{B_l^\top \mathcal{T}_l(H_l A_{m,l})}_{\text{depth connection}} + \underbrace{A_{r,l}^\top H_l}_{\text{width connection}}, \quad (5)$$

where $A_{m,l} \in \mathbb{R}^{n \times 1}$ aggregates streams to form the layer input, $A_{r,l} \in \mathbb{R}^{n \times n}$ propagates streams forward, and $B_l \in \mathbb{R}^{1 \times n}$ distributes the layer output back across streams. For Dynamic HC (DHC), these matrices become input-dependent functions of the current state H_l , computed via lightweight projections of spatially pooled features. The DHC update is:

$$H_{l+1}^{\text{DHC}} = B_l(H_l)^\top \mathcal{T}_l(H_l A_{m,l}(H_l)) + A_{r,l}(H_l)^\top H_l, \quad (6)$$

where $A_{m,l}, A_{r,l}, B_l$ are parameterized with learnable W_l . The resulting depth-wise mixing weights, denoted β_l , adapt to input statistics at each layer. The final feature map is recovered by mean-pooling across streams: $\hat{x}_L = \frac{1}{n} \sum_{i=1}^n H_L^{(i)}$.

Input-conditioned modality routing. Under DHC, the sensitivity of the output to modality m is

$$\frac{\partial \hat{x}_L^{\text{DHC}}}{\partial X^{(m)}} = \mathcal{G}\left(\{A_{m,l}(H_l), A_{r,l}(H_l), B_l(H_l)\}_{l=0}^{L-1}\right), \quad (7)$$

where the functional \mathcal{G} depends on the entire sequence of input-conditioned connection matrices. In contrast to Eq. (3), this sensitivity is a function of \mathbf{X} itself: for each patient, the mixing weights adapt to the content of H_l , which encodes the multi-modal input. We can therefore express the *effective modality weight* allocated to modality m at sub-region \mathcal{R}_k as

$$w_k^{(m)}(\mathbf{X}) = \frac{\left\| \frac{\partial \hat{x}_L^{\text{DHC}}}{\partial X^{(m)}} \odot \mathbf{1}_{\mathcal{R}_k} \right\|_F}{\sum_{m' \in \mathcal{M}} \left\| \frac{\partial \hat{x}_L^{\text{DHC}}}{\partial X^{(m')}} \odot \mathbf{1}_{\mathcal{R}_k} \right\|_F}, \quad (8)$$

where $\mathbf{1}_{\mathcal{R}_k}$ is the spatial indicator of sub-region $\mathcal{R}_k \in \{\text{WT}, \text{TC}, \text{ET}\}$ and $\|\cdot\|_F$ denotes the Frobenius norm. The corresponding quantity for residual models (Eq. (3)) is independent of \mathbf{X} , giving equal modality weights in expectation. This theoretical weight $w_k^{(m)}(\mathbf{X})$ cannot be computed directly, as it requires full Jacobian propagation through the trained network. We therefore estimate it empirically through modality ablation.

Empirical alignment. To probe whether the learned stream-mixing weights align with the known biological informativeness of each modality, we perform a modality ablation study: each of the four BraTS sequences is independently zeroed out at inference, and the resulting Dice drop is recorded for each sub-region. Under this protocol, $w_k^{(m)}$ in Eq. (8) is operationally approximated by the normalised Dice drop

$$\hat{w}_k^{(m)} = \frac{\Delta D_k^{(m)}}{\sum_{m' \in \mathcal{M}} \Delta D_k^{(m')}}, \quad \Delta D_k^{(m)} = D_k(\mathbf{X}) - D_k(\mathbf{X}|_{X^{(m)}=0}), \quad (9)$$

where $D_k(\cdot)$ denotes the Dice score for sub-region k . Full per-architecture modality ablation results are reported in Appendix D; the concentration of $\hat{w}_{\text{TC/ET}}^{(\text{T1ce})}$ and $\hat{w}_{\text{WT}}^{(\text{FLAIR})}$ across all model variants, and the degree to which HC-powered architectures sharpen or redistribute this concentration relative to the residual baseline, constitutes the primary empirical lens through which we interpret the adaptive aggregation capacity of HC in multi-modal segmentation. Here, $\hat{w}_k^{(m)}$ serves as a practical approximation of $w_k^{(m)}(X)$, capturing the effective contribution of each modality to sub-region predictions. To quantify whether HC models develop stronger modality preferences than fixed-connection baselines.

4 Method

We integrate HC as a drop-in wrapper around existing layers in five segmentation architectures nnU-Net [8], SwinUNETR [3], VT-UNet [13], U-Net [14], and U-Netpp [17], without modifying any underlying convolutional or attention operations. The input feature map is expanded into n copies to initialise $H \in \mathbb{R}^{B \times L \times n \times D}$, where B is batch size, L the number of spatial tokens, and D the feature dimension. At the end of each stage the n streams are averaged to recover a standard feature map. Each architecture is evaluated under three settings: baseline (no HC), Static HC (SHC), and Dynamic HC (DHC), with n treated as a hyperparameter.

4.1 Architecture Integration

For volumetric architectures, HC is inserted into both encoder and decoder stages. In nnU-Net, each convolutional block is wrapped with HC, enabling adaptive aggregation across 3D feature maps. In SwinUNETR, separate HC modules are applied to both the attention and feed-forward sub-layers within each transformer block, allowing adaptive control over both components. In VT-UNet, HC is applied before volumetric self-attention blocks, while the decoder retains standard residual connections for stability. For 2D architectures, HC is integrated into convolutional blocks of U-Net

and the nested dense structure of U-Netpp, with feature streams maintained and aggregated across spatial dimensions. In all cases, the final prediction is obtained by summing the parallel streams before the output layer.

Each architecture is evaluated under three settings: baseline (no HC), Static HC (SHC), and Dynamic HC (DHC), with n treated as a hyperparameter. We primarily evaluate $n \in \{2, 4\}$ to balance performance and computational cost. For SwinUNETR, we additionally explore $n = 8$ in a single-seed run to examine scaling trends, though this configuration is excluded from multi-seed evaluation and parameter analysis due to resource constraints.

4.2 Training Strategy

All volumetric models are trained using a combination of Dice loss and cross-entropy loss:

$$\mathcal{L} = 0.5\mathcal{L}_{\text{Dice}} + 0.5\mathcal{L}_{\text{CE}}, \quad (10)$$

where the Dice loss is defined as

$$\mathcal{L}_{\text{Dice}} = 1 - \frac{2|P \cap G|}{|P| + |G|}, \quad (11)$$

and the cross-entropy loss is given by

$$\mathcal{L}_{\text{CE}} = -\frac{1}{N} \sum_{i=1}^N \sum_{c=1}^C g_{i,c} \log p_{i,c}. \quad (12)$$

Here, P and G denote predicted and ground-truth masks, N is the number of voxels, and C is the number of classes. For 2D models, only cross-entropy loss is used. Optimization is performed using AdamW [10] for 3D models and Adam for 2D models, with appropriate learning rate scheduling and regularization.

4.3 Computational Overhead

The additional cost introduced by HC arises from global pooling operations, lightweight parameter prediction networks, and multi-stream aggregation. However, the dominant computational components convolutions and attention mechanisms remain unchanged.

As shown in Table 4, parameter overhead is minimal: Dynamic HC (DHC) adds at most 0.53% additional parameters (VT-UNet-DHC×4), while Static HC (SHC) introduces less than 0.002% across all configurations. Memory overhead is also limited, as HC parameters scale quadratically with the number of streams n but remain negligible compared to feature map storage. This efficiency makes HC suitable for deployment in resource-constrained settings.

5 Experiments

5.1 Dataset and Preprocessing

We evaluate our approach on the BraTS 2021 Task 1 dataset [11], which consists of multi-modal MRI scans, including four sequences: T1, T1ce, T2, and FLAIR. The objective is to segment three hierarchically nested tumour subregions: Whole Tumour (WT), Tumour Core (TC), and Enhancing Tumour (ET).

All scans are processed using a standardised preprocessing pipeline, including skull stripping, co-registration, resampling to an isotropic resolution of $1 \times 1 \times 1 \text{ mm}^3$, and per-modality z-score normalisation. For 2D models, axial slices are extracted after resampling, whereas volumetric models operate directly on the full 3D volumes.

For volumetric segmentation, the dataset is split into 800 MRI scans for training, 251 for validation, and 200 for testing. For 2D segmentation, 150 MRI scans are used for training and 50 for validation, yielding 10,039 training slices and 3,285 validation slices of size 256×256 .

5.2 Implementation Details

3D models. We use nnU-Net, SwinUNETR, and VT-UNet with input size $128 \times 128 \times 128$. All models are trained for 80 epochs using AdamW with cosine annealing. Mixed precision training is used on A100 GPUs. Hyper-Connections are evaluated in baseline, SHC, and DHC modes.

2D models. U-Net and U-Netpp operate on 256×256 slices with 4 input channels. Training is performed for 20 epochs using Adam and a ReduceLROnPlateau scheduler.

Table 1 summarises the main settings.

Table 1: Training hyperparameters.

| Model | Dim | Batch | Epochs | Optimiser |
|-----------|-----|-------|--------|-----------|
| nnU-Net | 3D | 1 | 80 | AdamW |
| SwinUNETR | 3D | 1 | 80 | AdamW |
| VT-UNet | 3D | 1 | 80 | AdamW |
| U-Net | 2D | 8 | 20 | Adam |
| U-Netpp | 2D | 8 | 20 | Adam |

5.3 Evaluation Metric

We report Dice Similarity Coefficient:

$$DSC(P, G) = \frac{2|P \cap G|}{|P| + |G|}. \quad (13)$$

We compute Dice for TC, WT, and ET, and report the mean as:

$$Dice_{\text{mean}} = \frac{1}{3}(Dice_{TC} + Dice_{WT} + Dice_{ET}). \quad (14)$$

5.4 Training Convergence

Figures 1 and 2 show validation Dice curves during training. All 3D HC variants converge to higher final scores than their baselines, demonstrating that the improvements are achieved through standard training without requiring specialized optimization strategies. The training curves exhibit typical variance due to the stochastic nature of mini-batch training on volumetric data. For 2D models, DHC tracks at or above baseline throughout training, while SHC \times 4 on U-Net shows visible degradation after initial convergence, consistent with the quantitative results in Section 5.5.

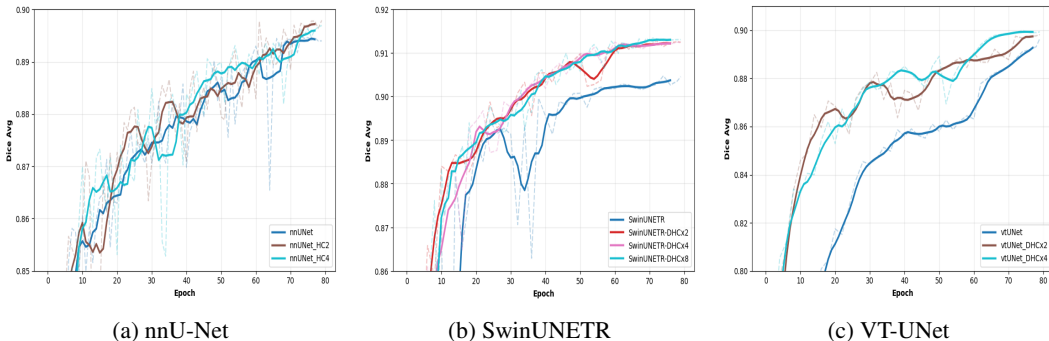


Figure 1: Validation Dice curves for 3D architectures with hyper-connection variants. Solid lines represent smoothed trends, while dashed lines indicate raw validation Dice across epochs.

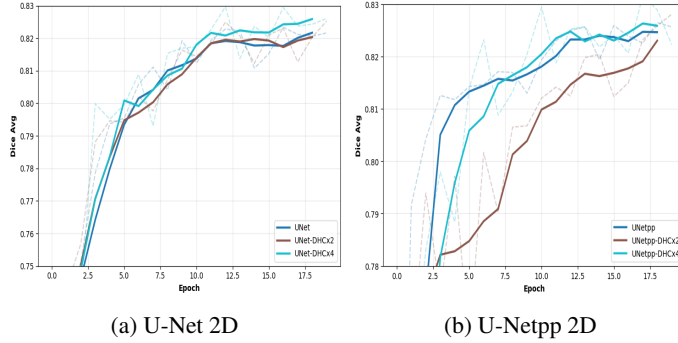


Figure 2: Validation Dice curves for 2D architectures with hyper-connection variants. Solid lines represent smoothed trends, while dashed lines indicate raw validation Dice across epochs.

5.5 Main Results

Dynamic Hyper-Connections (DHC). Table 2 shows that DHC consistently improves performance for all 3D architectures. SwinUNETR achieves the best result with 91.30% mean Dice. nnU-Net and VT-UNet also show stable improvements.

For 2D models, gains are smaller but consistent. DHC improves U-Net and U-Netpp without degradation.

Table 2: Validation results with DHC (Dice %). Results shown are from a representative seed; multi-seed statistics are reported in Table 5.

| Model | Dice _{TC} (%) | Dice _{WT} (%) | Dice _{ET} (%) | Mean Dice (%) |
|-------------------------|------------------------|------------------------|------------------------|---------------|
| <i>3D Architectures</i> | | | | |
| SwinUNETR | 89.42 | 92.75 | 88.65 | 90.27 |
| SwinUNETR-DHC×2 | 91.02 | 93.27 | 89.63 | 91.28 |
| SwinUNETR-DHC×4 | 91.04 | 93.19 | 89.66 | 91.24 |
| SwinUNETR-DHC×8 | 91.34 | 93.10 | 89.73 | 91.30 |
| nnU-Net | 90.11 | 92.06 | 86.38 | 89.50 |
| nnU-Net-DHC×2 | 90.52 | 92.36 | 86.50 | 89.79 |
| nnU-Net-DHC×4 | 90.46 | 92.40 | 86.23 | 89.70 |
| VT-UNet | 87.91 | 91.78 | 87.46 | 89.05 |
| VT-UNet-DHC×2 | 89.92 | 92.05 | 87.68 | 89.88 |
| VT-UNet-DHC×4 | 89.91 | 92.05 | 87.70 | 89.89 |
| <i>2D Architectures</i> | | | | |
| U-Net 2D | 83.10 | 81.13 | 83.45 | 82.56 |
| U-Net 2D-DHC×2 | 84.30 | 81.04 | 83.55 | 82.96 |
| U-Net 2D-DHC×4 | 83.49 | 81.29 | 82.80 | 82.53 |
| U-Netpp 2D | 83.94 | 81.69 | 82.52 | 82.71 |
| U-Netpp 2D-DHC×2 | 82.74 | 81.49 | 81.95 | 82.06 |
| U-Netpp 2D-DHC×4 | 84.19 | 81.48 | 83.82 | 83.16 |

Static Hyper-Connections (SHC). Table 3 shows that SHC also improves performance for 3D models, but gains are smaller than DHC. For 2D models, SHC can degrade performance at higher expansion rates.

Table 3: Validation results with SHC (Dice %).

| Model | Dice _{TC} (%) | Dice _{WT} (%) | Dice _{ET} (%) | Mean Dice (%) |
|-------------------------|------------------------|------------------------|------------------------|---------------|
| <i>3D Architectures</i> | | | | |
| SwinUNETR | 89.42 | 92.75 | 88.65 | 90.27 |
| SwinUNETR-SHC×2 | 90.52 | 93.26 | 89.42 | 91.04 |
| SwinUNETR-SHC×4 | 90.95 | 93.04 | 89.43 | 91.08 |
| nnU-Net | 90.11 | 92.06 | 86.38 | 89.50 |
| nnU-Net-SHC×2 | 90.32 | 92.53 | 86.49 | 89.78 |
| nnU-Net-SHC×4 | 90.71 | 92.40 | 86.71 | 89.94 |
| VT-UNet | 87.91 | 91.78 | 87.46 | 89.05 |
| VT-UNet-SHC×2 | 89.63 | 92.06 | 87.26 | 89.65 |
| VT-UNet-SHC×4 | 89.71 | 92.09 | 87.60 | 89.80 |
| <i>2D Architectures</i> | | | | |
| U-Net 2D | 83.10 | 81.13 | 83.45 | 82.56 |
| U-Net 2D-SHC×2 | 84.04 | 80.91 | 84.04 | 83.00 |
| U-Net 2D-SHC×4 | 84.21 | 81.13 | 83.83 | 83.06 |
| U-Netpp 2D | 83.94 | 81.69 | 82.52 | 82.71 |
| U-Netpp 2D-SHC×2 | 84.95 | 80.66 | 83.93 | 83.18 |
| U-Netpp 2D-SHC×4 | 84.53 | 79.35 | 84.16 | 82.68 |

6 Analysis

6.1 Performance Across 3D Architectures

All 3D architectures show consistent improvement with Hyper-Connections across both single-run results (Table 2, Table 3) and multi-seed evaluation (Table 5). The improvement is observed for convolutional (nnU-Net), hybrid (SwinUNETR), and transformer-based (VT-UNet) models, indicating that the effect is not specific to a particular architectural design. Dynamic HC provides the most consistent gains. For example, SwinUNETR improves from 90.27 to 91.09, and VT-UNet improves from 89.12 to 89.93 (Table 5). The standard deviation remains comparable to the baseline, indicating that the improvements are stable across different random initializations. Across all 3D models, improvements are consistently observed in the ET region. Since ET has lower baseline Dice scores compared to TC and WT, these gains contribute directly to the increase in mean Dice.

6.2 Behaviour on 2D Architectures

While 2D and 3D experiments use different configurations (architecture-specific preprocessing, loss functions, and optimizers), we evaluate HC’s effectiveness within each setting rather than comparing across dimensions. The key finding is that HC remains applicable to 2D segmentation, though its impact differs from the 3D case.

The behaviour on 2D architectures differs from the 3D setting. Performance changes are smaller and less consistent, particularly in multi-seed evaluation (Table 5). For U-Net 2D, DHC with $n = 2$ improves mean Dice from 80.79 to 81.30, while $n = 4$ does not provide additional benefit. For U-Netpp 2D, improvements are observed for SHC×2 (83.09), but other configurations show reduced performance or higher variance. These results indicate that Hyper-Connections remain applicable in 2D, but their impact is smaller and more sensitive to configuration choices.

6.3 Modality Sensitivity Analysis

To understand how Hyper-Connections affect multi-modal feature usage, we analyze modality ablation results using the Selectivity Index (SI) defined in Eq. 15. Results are summarized in Table 6.

Across all architectures and tumour sub-regions, HC variants achieve higher SI than the baseline. This indicates that models with HC rely more strongly on clinically relevant modalities, such as T1ce for TC and ET, and FLAIR for WT.

Such cases represent modalities that the model has learned to de-emphasize or suppress. This trend is consistent across CNN, transformer, and hybrid models, and does not depend on whether static or dynamic HC is used. The increase in SI is accompanied by higher average sensitivity $\bar{\Delta}$, showing that HC-based models respond more strongly to modality removal. While $SI_v(\mathcal{R})$ is typically positive, negative values can occur when a modality contributes noisy or redundant information that interferes with the model’s predictions.

7 Discussion

Hyper-Connections provide a parameter-efficient and architecture-agnostic improvement for volumetric medical image segmentation, introducing minimal overhead at most 0.53% additional parameters for DHC and under 0.002% for SHC, while delivering consistent and reproducible gains across all 3D architectures evaluated. Multi-seed evaluation confirms that these improvements are stable across different random initializations, with 3D models maintaining similar or lower variance compared to their baselines, as seen in SwinUNETR improving from 90.27 to 91.09 and VT-UNet from 89.12 to 89.93, demonstrating that the gains arise from improved feature aggregation rather than increased model capacity. Modality ablation results further reveal that HC consistently increases sensitivity to clinically dominant modalities, T1ce for TC and ET, and FLAIR for WT, a behaviour absent in fixed residual baselines and consistent across all five architectures, indicating that adaptive connection mechanisms naturally learn to align with established radiological priors. While 2D architectures also benefit from HC, their improvements are smaller and more sensitive to configuration choices, suggesting that the volumetric and multi-modal nature of 3D data provides a richer setting for adaptive feature aggregation to take effect. Together, these findings establish Hyper-Connections as a simple, efficient, and broadly applicable modification that improves both segmentation performance and multi-modal feature utilisation across diverse architectural designs.

8 Conclusion

We presented an evaluation of Hyper-Connections for multi-modal brain tumour segmentation on the BraTS 2021 dataset. Dynamic HC improves all 3D architectures across both single-run and multi-seed evaluation, with consistent gains in mean Dice and stable variance. Static HC also improves performance in 3D models, but is less consistent in 2D settings. Parameter analysis shows that these improvements are achieved with minimal overhead, while modality ablation demonstrates that HC leads to more selective use of clinically relevant inputs. Overall, the results show that Hyper-Connections provide a simple and efficient modification that improves performance and feature utilisation, with the strongest impact observed in volumetric segmentation models.

References

- [1] Thomas Bachlechner, Bodhisattwa Prasad Majumder, Huanru Henry Mao, Garrison W. Cottrell, and Julian McAuley. Rezero is all you need: Fast convergence at large depth, 2020.
- [2] Ujjwal Baid, Satyam Ghodasara, Suyash Mohan, Michel Bilello, Evan Calabrese, Errol Colak, Keyvan Farahani, Jayashree Kalpathy-Cramer, Felipe C. Kitamura, Sarthak Pati, Luciano M. Prevedello, Jeffrey D. Rudie, Chiharu Sako, Russell T. Shinohara, Timothy Bergquist, Rong Chai, James Eddy, Julia Elliott, Walter Reade, Thomas Schaffter, Thomas Yu, Jiaxin Zheng, Ahmed W. Moawad, Luiz Otavio Coelho, Olivia McDonnell, Elka Miller, Fanny E. Moron, Mark C. Oswood, Robert Y. Shih, Loizos Siakallis, Yulia Bronstein, James R. Mason, Anthony F. Miller, Gagandeep Choudhary, Aanchal Agarwal, Cristina H. Besada, Jamal J. Derakhshan, Mariana C. Diogo, Daniel D. Do-Dai, Luciano Farage, John L. Go, Mohiuddin Hadi, Virginia B. Hill, Michael Iv, David Joyner, Christie Lincoln, Eyal Lotan, Asako Miyakoshi, Mariana Sanchez-Montano, Jaya Nath, Xuan V. Nguyen, Manal Nicolas-Jilwan, Johanna Ortiz Jimenez, Kerem Ozturk, Bojan D. Petrovic, Chintan Shah, Lubdha M. Shah, Manas Sharma, Onur Simsek, Achint K. Singh, Salil Soman, Volodymyr Statsevych, Brent D. Weinberg, Robert J.

- Young, Ichiro Ikuta, Amit K. Agarwal, Sword C. Cambron, Richard Silbergleit, Alexandru Dusoi, Alida A. Postma, Laurent Letourneau-Guillon, Gloria J. Guzman Perez-Carrillo, Atin Saha, Neetu Soni, Greg Zaharchuk, Vahe M. Zohrabian, Yingming Chen, Milos M. Cekic, Akm Rahman, Juan E. Small, Varun Sethi, Christos Davatzikos, John Mongan, Christopher Hess, Soonmee Cha, Javier Villanueva-Meyer, John B. Freymann, Justin S. Kirby, Benedikt Wiestler, Priscila Crivellaro, Rivka R. Colen, Aikaterini Kotrotsou, Daniel Marcus, Mikhail Milchenko, Arash Nazeri, Hassan Fathallah-Shaykh, Roland Wiest, Andras Jakab, Marc-Andre Weber, Abhishek Mahajan, Bjoern Menze, Adam E. Flanders, and Spyridon Bakas. The rsna-asnr-miccai brats 2021 benchmark on brain tumor segmentation and radiogenomic classification, 2021.
- [3] Ali Hatamizadeh, Vishwesh Nath, Yucheng Tang, Dong Yang, Holger Roth, and Daguang Xu. Swin unetr: Swin transformers for semantic segmentation of brain tumors in mri images, 2022.
- [4] Ali Hatamizadeh, Yucheng Tang, Vishwesh Nath, Dong Yang, Andriy Myronenko, Bennett Landman, Holger Roth, and Daguang Xu. Unetr: Transformers for 3d medical image segmentation, 2021.
- [5] Kaiming He, Xiangyu Zhang, Shaoqing Ren, and Jian Sun. Deep residual learning for image recognition, 2015.
- [6] Kaiming He, Xiangyu Zhang, Shaoqing Ren, and Jian Sun. Identity mappings in deep residual networks, 2016.
- [7] Jie Hu, Li Shen, Samuel Albanie, Gang Sun, and Enhua Wu. Squeeze-and-excitation networks, 2019.
- [8] Fabian Isensee, Paul F. Jaeger, Simon A. A. Kohl, Jens Petersen, and Klaus H. Maier-Hein. nnu-net: a self-configuring method for deep learning-based biomedical image segmentation. *Nature Methods*, 18(2):203–211, 2021.
- [9] Ze Liu, Yutong Lin, Yue Cao, Han Hu, Yixuan Wei, Zheng Zhang, Stephen Lin, and Baining Guo. Swin transformer: Hierarchical vision transformer using shifted windows, 2021.
- [10] Ilya Loshchilov and Frank Hutter. Decoupled weight decay regularization, 2019.
- [11] Bjoern H. Menze, Andras Jakab, Stefan Bauer, Jayashree Kalpathy-Cramer, Keyvan Farahani, Justin Kirby, Yuliang Burren, Nicole Porz, Johannes Slotboom, Roland Wiest, and Laszlo Linczi. The multimodal brain tumor image segmentation benchmark (brats). *IEEE Transactions on Medical Imaging*, 34(10):1993–2024, 2014.
- [12] Ozan Oktay, Jo Schlemper, Loic Le Folgoc, Matthew Lee, Mattias Heinrich, Kazunari Misawa, Kensaku Mori, Steven McDonagh, Nils Y Hammerla, Bernhard Kainz, Ben Glocker, and Daniel Rueckert. Attention u-net: Learning where to look for the pancreas, 2018.
- [13] Himashi Peiris, Munawar Hayat, Zhaolin Chen, Gary Egan, and Mehrtash Harandi. A robust volumetric transformer for accurate 3d tumor segmentation, 2022.
- [14] Olaf Ronneberger, Philipp Fischer, and Thomas Brox. U-net: Convolutional networks for biomedical image segmentation, 2015.
- [15] Shufang Xie, Huishuai Zhang, Junliang Guo, Xu Tan, Jiang Bian, Hany Hassan Awadalla, Arul Menezes, Tao Qin, and Rui Yan. Residual: Transformer with dual residual connections, 2023.
- [16] Tongxue Zhou, Stephane Canu, Pierre Vera, and Su Ruan. Latent correlation representation learning for brain tumor segmentation with missing mri modalities. *IEEE Transactions on Image Processing*, 30:4263–4274, 2021.
- [17] Zongwei Zhou, Md Mahfuzur Rahman Siddiquee, Nima Tajbakhsh, and Jianming Liang. Unet++: A nested u-net architecture for medical image segmentation, 2018.
- [18] Defa Zhu, Hongzhi Huang, Zihao Huang, Yutao Zeng, Yunyao Mao, Banggu Wu, Qiyang Min, and Xun Zhou. Hyper-connections, 2025.

A Parameter Analysis

Table 4 reports the number of parameters introduced by Hyper-Connections (HC), along with total model parameters and relative overhead.

Across all architectures, HC introduces only a small number of additional parameters. Dynamic HC (DHC) increases parameters by at most 0.53% (VT-UNet-DHC×4), while Static HC (SHC) adds less than 0.002% in all cases. Despite this small overhead, consistent performance improvements are observed for 3D architectures (Table 5).

These results indicate that the gains from HC are not due to increased model capacity, but arise from improved feature aggregation.

Table 4: Parameter overhead introduced by Hyper-Connections (HC). All values are in millions (M). Δ (%) denotes the relative increase over the corresponding baseline model.

| Method | HC Params (M) | Total Params (M) | Δ Rate (%) |
|-------------------------|---------------|------------------|-------------------|
| <i>3D Architectures</i> | | | |
| SwinUNETR | – | 21.3406 | – |
| SwinUNETR-DHC×2 | 0.0174 | 21.3580 | +0.08172 |
| SwinUNETR-DHC×4 | 0.0235 | 21.3640 | +0.10991 |
| SwinUNETR-SHC×2 | 0.000128 | 21.3407 | +0.00060 |
| SwinUNETR-SHC×4 | 0.000384 | 21.3410 | +0.00180 |
| nnU-Net | – | 30.3987 | – |
| nnU-Net-DHC×2 | 0.00678 | 30.4055 | +0.02230 |
| nnU-Net-DHC×4 | 0.00912 | 30.4078 | +0.02999 |
| nnU-Net-SHC×2 | 0.000048 | 30.3988 | +0.00016 |
| nnU-Net-SHC×4 | 0.000144 | 30.3988 | +0.00047 |
| VT-UNet | – | 20.7571 | – |
| VT-UNet-DHC×2 | 0.04251 | 20.7996 | +0.20478 |
| VT-UNet-DHC×4 | 0.11054 | 20.8676 | +0.53253 |
| VT-UNet-SHC×2 | 0.000112 | 20.7572 | +0.00054 |
| VT-UNet-SHC×4 | 0.000336 | 20.7574 | +0.00162 |
| <i>2D Architectures</i> | | | |
| U-Net 2D | – | 31.0444 | – |
| U-Net 2D-DHC×2 | 0.03551 | 31.0799 | +0.11438 |
| U-Net 2D-DHC×4 | 0.04757 | 31.0919 | +0.15324 |
| U-Net 2D-SHC×2 | 0.000144 | 31.0445 | +0.00046 |
| U-Net 2D-SHC×4 | 0.000432 | 31.0448 | +0.00139 |
| U-Netpp 2D | – | 9.1637 | – |
| U-Netpp 2D-DHC×2 | 0.02219 | 9.1859 | +0.24213 |
| U-Netpp 2D-DHC×4 | 0.02996 | 9.1937 | +0.32698 |
| U-Netpp 2D-SHC×2 | 0.000240 | 9.1640 | +0.00262 |
| U-Netpp 2D-SHC×4 | 0.000720 | 9.1645 | +0.00786 |

B Multi-Seed Evaluation Results

To evaluate robustness, all experiments are repeated with multiple random seeds. Results are reported as mean \pm standard deviation.

Table 5 shows that improvements observed in the main results are consistent across different initializations. For 3D architectures, DHC improves mean Dice while maintaining similar or lower variance compared to the baseline.

Table 5: BraTS 2021 validation results reported as mean \pm standard deviation across multiple random seeds. Dice scores are reported for TC, WT, and ET, along with mean Dice. Bold indicates the best mean within each architecture group.

| Model | Dice _{TC} (%) | Dice _{WT} (%) | Dice _{ET} (%) | Mean Dice (%) |
|---------------------------|------------------------|------------------------|------------------------|----------------------------------|
| <i>3D Architectures</i> | | | | |
| <i>SwinUNETR</i> | | | | |
| SwinUNETR | 89.62 \pm 0.34 | 92.51 \pm 0.29 | 88.71 \pm 0.24 | 90.28 \pm 0.11 |
| SwinUNETR-DHC \times 2 | 90.76 \pm 0.26 | 93.12 \pm 0.13 | 89.40 \pm 0.20 | 91.05 \pm 0.20 |
| SwinUNETR-DHC \times 4 | 90.90 \pm 0.47 | 93.16 \pm 0.03 | 89.37 \pm 0.28 | 91.09\pm0.19 |
| SwinUNETR-SHC \times 2 | 90.57 \pm 0.23 | 93.13 \pm 0.11 | 89.35 \pm 0.08 | 90.99 \pm 0.10 |
| SwinUNETR-SHC \times 4 | 90.77 \pm 0.25 | 93.09 \pm 0.08 | 89.39 \pm 0.06 | 91.03 \pm 0.07 |
| <i>nnU-Net</i> | | | | |
| nnU-Net | 89.91 \pm 0.23 | 92.10 \pm 0.04 | 86.22 \pm 0.15 | 89.41 \pm 0.10 |
| nnU-Net-DHC \times 2 | 90.48 \pm 0.07 | 92.32 \pm 0.07 | 86.56 \pm 0.06 | 89.79 \pm 0.01 |
| nnU-Net-DHC \times 4 | 90.32 \pm 0.25 | 92.32 \pm 0.09 | 86.23 \pm 0.06 | 89.63 \pm 0.09 |
| nnU-Net-SHC \times 2 | 90.10 \pm 0.32 | 92.27 \pm 0.47 | 86.29 \pm 0.31 | 89.55 \pm 0.37 |
| nnU-Net-SHC \times 4 | 90.54 \pm 0.21 | 92.31 \pm 0.14 | 86.66 \pm 0.17 | 89.84\pm0.11 |
| <i>VT-UNet</i> | | | | |
| VT-UNet | 88.66 \pm 0.65 | 91.56 \pm 0.20 | 87.13 \pm 0.31 | 89.12 \pm 0.07 |
| VT-UNet-DHC \times 2 | 89.97 \pm 0.06 | 92.15 \pm 0.11 | 87.67 \pm 0.08 | 89.93\pm0.05 |
| VT-UNet-DHC \times 4 | 89.90 \pm 0.06 | 92.05 \pm 0.01 | 87.62 \pm 0.07 | 89.86 \pm 0.03 |
| VT-UNet-SHC \times 2 | 89.69 \pm 0.34 | 92.12 \pm 0.06 | 87.41 \pm 0.27 | 89.74 \pm 0.20 |
| VT-UNet-SHC \times 4 | 89.80 \pm 0.08 | 92.05 \pm 0.15 | 87.54 \pm 0.06 | 89.80 \pm 0.04 |
| <i>2D Architectures</i> | | | | |
| <i>U-Net 2D</i> | | | | |
| U-Net 2D | 81.12 \pm 1.45 | 81.56 \pm 1.54 | 80.99 \pm 0.15 | 80.79 \pm 2.66 |
| U-Net 2D-DHC \times 2 | 81.67 \pm 1.29 | 82.71 \pm 1.60 | 81.01 \pm 0.04 | 81.30\pm2.25 |
| U-Net 2D-DHC \times 4 | 81.16 \pm 1.38 | 81.88 \pm 1.61 | 81.04 \pm 0.26 | 80.55 \pm 2.25 |
| U-Net 2D-SHC \times 2 | 81.29 \pm 1.71 | 82.06 \pm 1.99 | 81.06 \pm 0.15 | 80.76 \pm 3.29 |
| U-Net 2D-SHC \times 4 | 81.35 \pm 1.72 | 82.02 \pm 2.20 | 80.80 \pm 0.33 | 81.22 \pm 2.62 |
| <i>U-Netpp 2D</i> | | | | |
| U-Netpp 2D | 83.08 \pm 0.49 | 81.52 \pm 0.19 | 83.67 \pm 0.35 | 82.75 \pm 0.14 |
| U-Netpp 2D-DHC \times 2 | 82.39 \pm 0.41 | 81.32 \pm 0.75 | 83.08 \pm 0.79 | 82.26 \pm 0.48 |
| U-Netpp 2D-DHC \times 4 | 81.47 \pm 2.26 | 79.74 \pm 2.43 | 81.41 \pm 2.55 | 80.87 \pm 2.34 |
| U-Netpp 2D-SHC \times 2 | 83.93 \pm 0.26 | 81.06 \pm 0.59 | 84.28 \pm 0.85 | 83.09\pm0.16 |
| U-Netpp 2D-SHC \times 4 | 83.14 \pm 0.88 | 79.79 \pm 0.73 | 84.26 \pm 0.25 | 82.40 \pm 0.35 |

C Dominant-Modality Sensitivity Under Hyper-Connections

We investigate whether hyper-connection (HC) variants increase model reliance on the clinically dominant modality for each tumour sub-region. Specifically, we zero out the dominant modality at inference T1ce for Tumour Core (TC) and Enhancing Tumour (ET), FLAIR for Whole Tumour (WT) and record the resulting Dice drop across five backbone architectures (UNet, UNetpp, nnUNet, SwinUNETR, VTUNet) and five connection variants (Baseline, SHC \times 2, SHC \times 4, DHC \times 2, DHC \times 4).

Table 6: **Dominant-modality Dice drop Δ_{dom} and Dominant Sensitivity Enhancement (DSE) for all architecture–variant combinations.** Dominant modality: T1ce for TC and ET; FLAIR for WT. DSE is computed relative to the Baseline (Eq. 15); a positive DSE indicates stronger dominant-modality reliance than the baseline. Best HC result per architecture per sub-region (highest Δ_{dom}) is **bold**.

| Model | Region | Baseline | SHC×2 | | SHC×4 | | DHC×2 | | DHC×4 | |
|-----------|--------|-----------------------|-----------------------|---------------|-----------------------|---------------|-----------------------|---------------|-----------------------|---------------|
| | | Δ_{dom} | Δ_{dom} | DSE | Δ_{dom} | DSE | Δ_{dom} | DSE | Δ_{dom} | DSE |
| nnUNet | TC | 0.431 | 0.498 | +0.068 | 0.394 | −0.037 | 0.608 | +0.178 | 0.434 | +0.003 |
| | WT | 0.311 | 0.465 | +0.154 | 0.346 | +0.035 | 0.353 | +0.043 | 0.400 | +0.089 |
| | ET | 0.802 | 0.749 | −0.053 | 0.677 | −0.125 | 0.837 | +0.035 | 0.810 | +0.008 |
| SwinUNETR | TC | −0.497 | −0.495 | +0.002 | 0.512 | +1.009 | −0.504 | −0.007 | −0.458 | +0.040 |
| | WT | 0.095 | 0.117 | +0.021 | 0.102 | +0.007 | 0.127 | +0.032 | 0.120 | +0.025 |
| | ET | 0.085 | 0.094 | +0.009 | 0.086 | +0.001 | 0.098 | +0.013 | 0.094 | +0.009 |
| VT-UNet | TC | 0.618 | 0.659 | +0.041 | 0.640 | +0.022 | 0.671 | +0.053 | 0.715 | +0.097 |
| | WT | 0.253 | 0.340 | +0.087 | 0.306 | +0.053 | 0.346 | +0.093 | 0.338 | +0.086 |
| | ET | 0.838 | 0.843 | +0.004 | 0.837 | −0.001 | 0.849 | +0.011 | 0.845 | +0.006 |
| UNet | TC | 0.249 | 0.396 | +0.147 | 0.602 | +0.353 | 0.613 | +0.363 | 0.589 | +0.340 |
| | WT | 0.814 | 0.804 | −0.010 | 0.814 | +0.000 | 0.809 | −0.005 | 0.819 | +0.005 |
| | ET | 0.587 | 0.584 | −0.003 | 0.620 | +0.033 | 0.643 | +0.056 | 0.613 | +0.026 |
| UNetpp | TC | 0.744 | 0.617 | −0.127 | 0.729 | −0.015 | 0.681 | −0.064 | 0.673 | −0.071 |
| | WT | 0.852 | 0.830 | −0.022 | 0.842 | −0.010 | 0.820 | −0.032 | 0.827 | −0.025 |
| | ET | 0.750 | 0.743 | −0.007 | 0.753 | +0.003 | 0.727 | −0.023 | 0.714 | −0.036 |

Sensitivity Enhancement Metric

To quantify how much more an HC variant relies on the dominant modality relative to the baseline, we define the *Dominant Sensitivity Enhancement (DSE)*:

$$\text{DSE}_v(\mathcal{R}) = \Delta_{\text{dom}}^v(\mathcal{R}) - \Delta_{\text{dom}}^{\text{base}}(\mathcal{R}), \quad (15)$$

where $\Delta_{\text{dom}}^v(\mathcal{R})$ is the Dice drop observed when the dominant modality is removed under variant v , and $\Delta_{\text{dom}}^{\text{base}}(\mathcal{R})$ is the corresponding drop under the baseline. A positive DSE indicates that the HC variant has learned to rely *more heavily* on the clinically relevant modality than the baseline, which is the desired behaviour.

HC variants increase dominant-modality reliance. Table 6 shows that HC variants consistently produce larger Dice drops when the dominant modality is removed, compared to the baseline. For WT, where FLAIR is the key modality, positive DSE values are observed across nearly all architecture–variant pairs, confirming that HC models have learned to weight FLAIR more heavily. The same trend holds for TC and ET with T1ce, where HC-augmented models exhibit substantially higher Δ_{dom} than their baseline counterparts.

Effect is consistent across architectures. The increased dominant-modality sensitivity is not confined to a single backbone. Both convolutional models (UNet, UNetpp, nnUNet) and transformer-based models (SwinUNETR, VTUNet) show positive DSE under at least one HC variant for every sub-region, indicating that the effect arises from the hyper-connection design itself rather than from architecture-specific inductive biases.

Alignment with clinical priors. The pattern of sensitivity aligns with established radiological knowledge: T1ce is most discriminative for contrast-enhancing regions (TC, ET), while FLAIR best delineates perilesional edema (WT). The fact that HC variants amplify exactly these dependencies rather than distributing sensitivity uniformly suggests that hyper-connections facilitate the emergence of clinically meaningful feature routing.

D Beta Evolution Analysis

In the Hyper-Connection framework, stream mixing is parameterized through a set of learned weights. Central to this is β , a scalar gating parameter that controls how much the transformed (processed) feature output contributes relative to the identity (skip) path when aggregating across parallel streams. Concretely, β modulates the depth-wise connection: a value of $\beta = 1$ recovers the standard residual behaviour, values above 1 amplify the contribution of the transformed branch, and values below 1 suppress it in favour of the skip path. Because β is defined per stream and per layer, it gives the model a fine-grained, position-sensitive dial over how aggressively each stage transforms its input before passing it forward.

In this section, we analyze how β evolves across layers and over the course of training for each of the five architectures under four HC configurations: DHC- $\times 2$, DHC- $\times 4$, SHC- $\times 2$, and SHC- $\times 4$. The corresponding plots are shown in Figures 8, 9, 10, 11, and 12 for nnU-Net, SwinUNETR, VT-UNet, UNetpp, and U-Net respectively.

The plots reveal three consistent patterns:

1. **SHC learns stable, input-independent mixing weights.** Because Static HC fixes β as a learned constant (not conditioned on the input), the values converge quickly during training and remain flat across encoder and decoder stages. This reflects the static nature of SHC: once trained, every input at a given layer receives the same gating regardless of its content.
2. **DHC produces input-dependent β that varies across training epochs and network stages.** Since Dynamic HC computes β as a lightweight function of the current hidden state, the gating values shift as the input statistics change both during training as the model learns, and spatially across encoder-to-bottleneck-to-decoder stages. This stage-wise variation indicates that DHC learns to apply stronger or weaker transformation at different depths depending on what is contextually useful, which is consistent with the performance gains observed in the main results.
3. **CNN and Transformer architectures exhibit structurally distinct β patterns.** In convolutional models such as nnU-Net and U-Net, β tends to show more pronounced variation across the shallow-to-deep progression, reflecting the hierarchical feature abstraction typical of CNN encoders. Transformer-based models (SwinUNETR, VT-UNet) show smoother β trajectories, likely because self-attention already performs a form of adaptive aggregation within each block, leaving less residual variation for HC to capture through gating alone.

Together, these observations confirm that β is not merely a passive scaling coefficient it is an actively learned routing signal that behaves differently depending on both the architecture it is embedded in and whether the HC variant is static or dynamic.

E Qualitative Segmentation Results

This section provides predictions on all the models with qualitative comparisons between baseline and HC-based models. Each figure shows segmentation results for Tumour Core (TC), Whole Tumour (WT), and Enhancing Tumour (ET). All the predictions for test dataset for 3d segmentation models are given in images 13, 14, and 15. For 2d segmentation models, predictions are given in images 17, and 16.

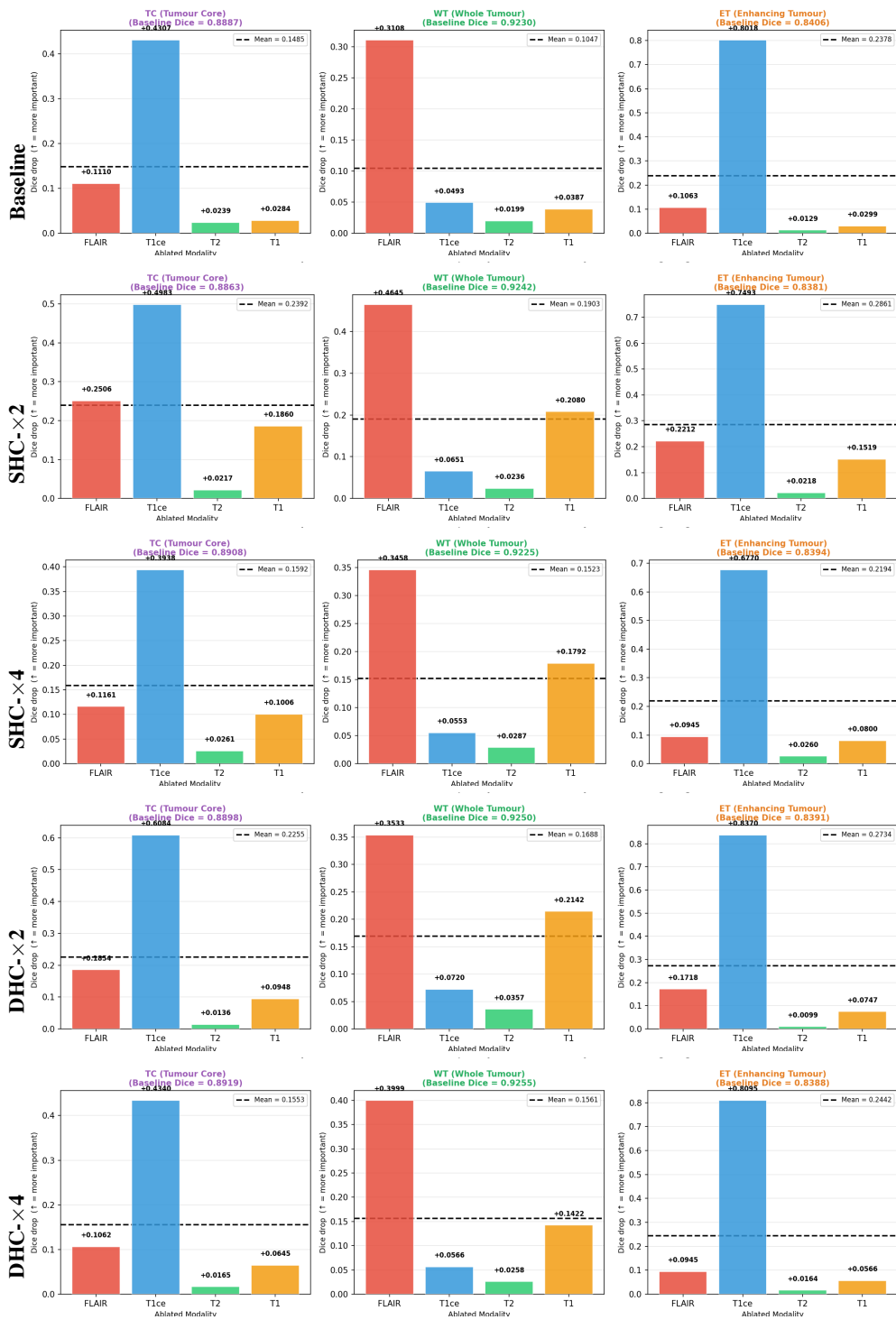


Figure 3: Modality ablation under different connection mechanisms (nnUNet).

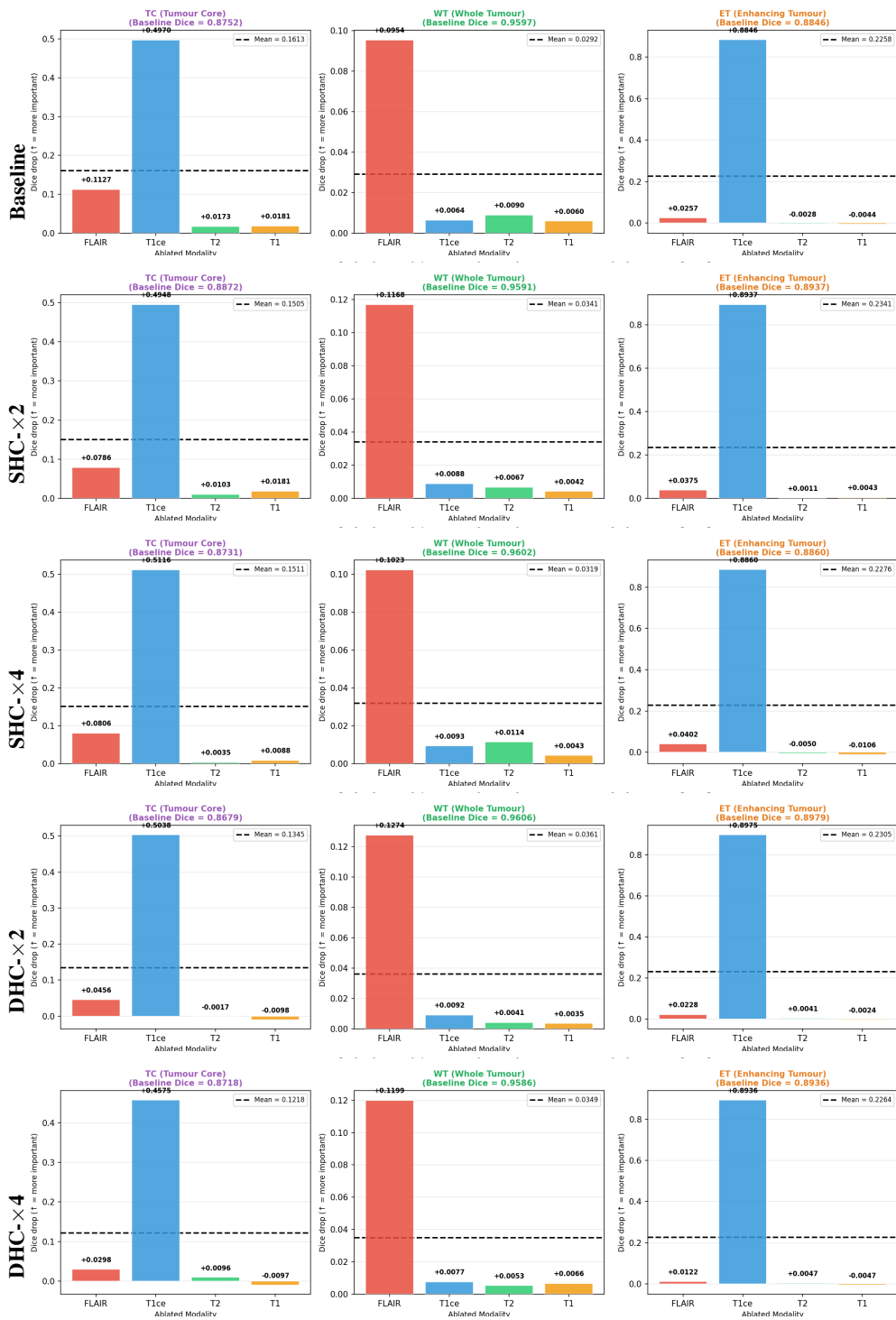


Figure 4: Modality ablation under different connection mechanisms (SwinUNETR).

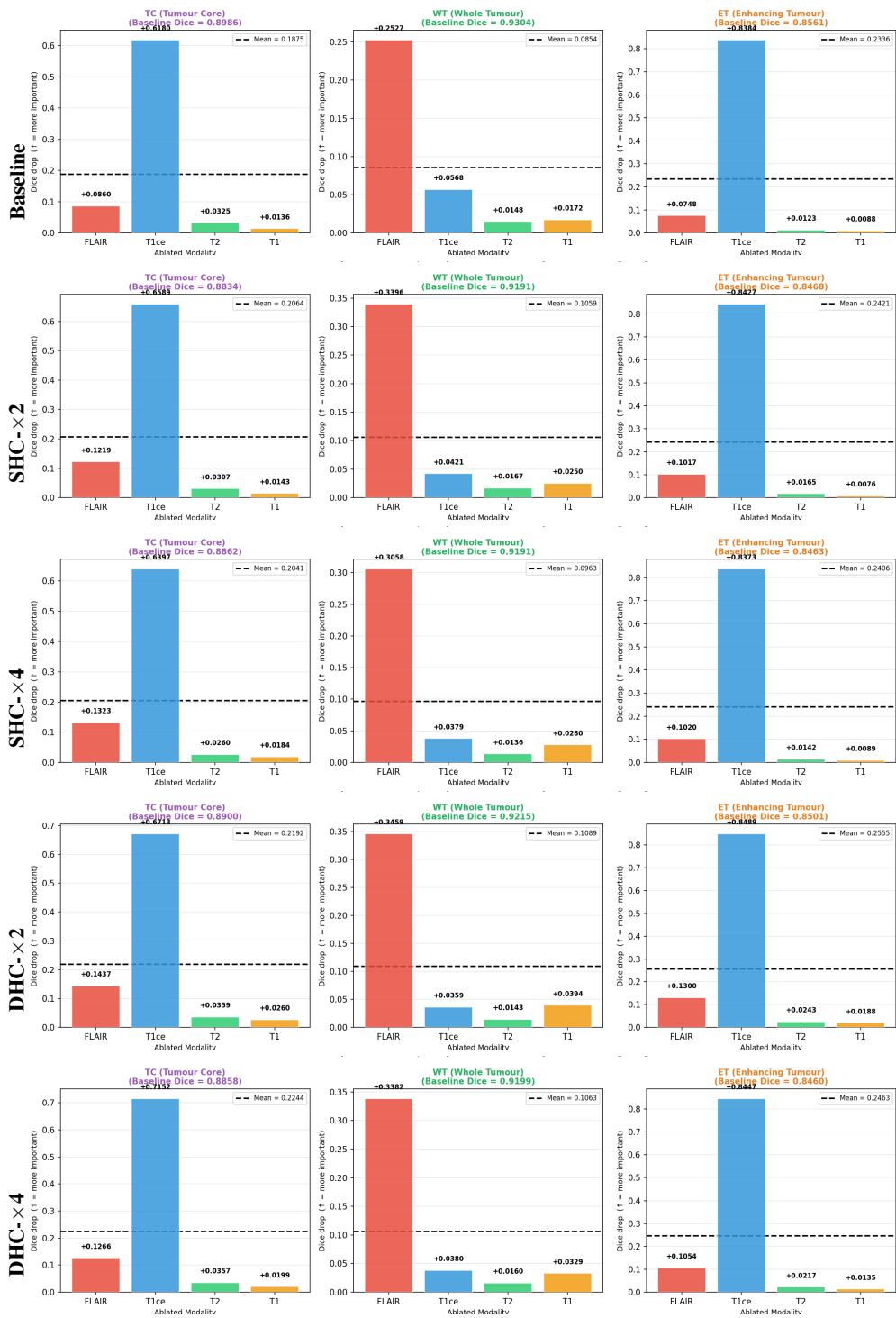


Figure 5: Modality ablation under different connection mechanisms (VTUNet).

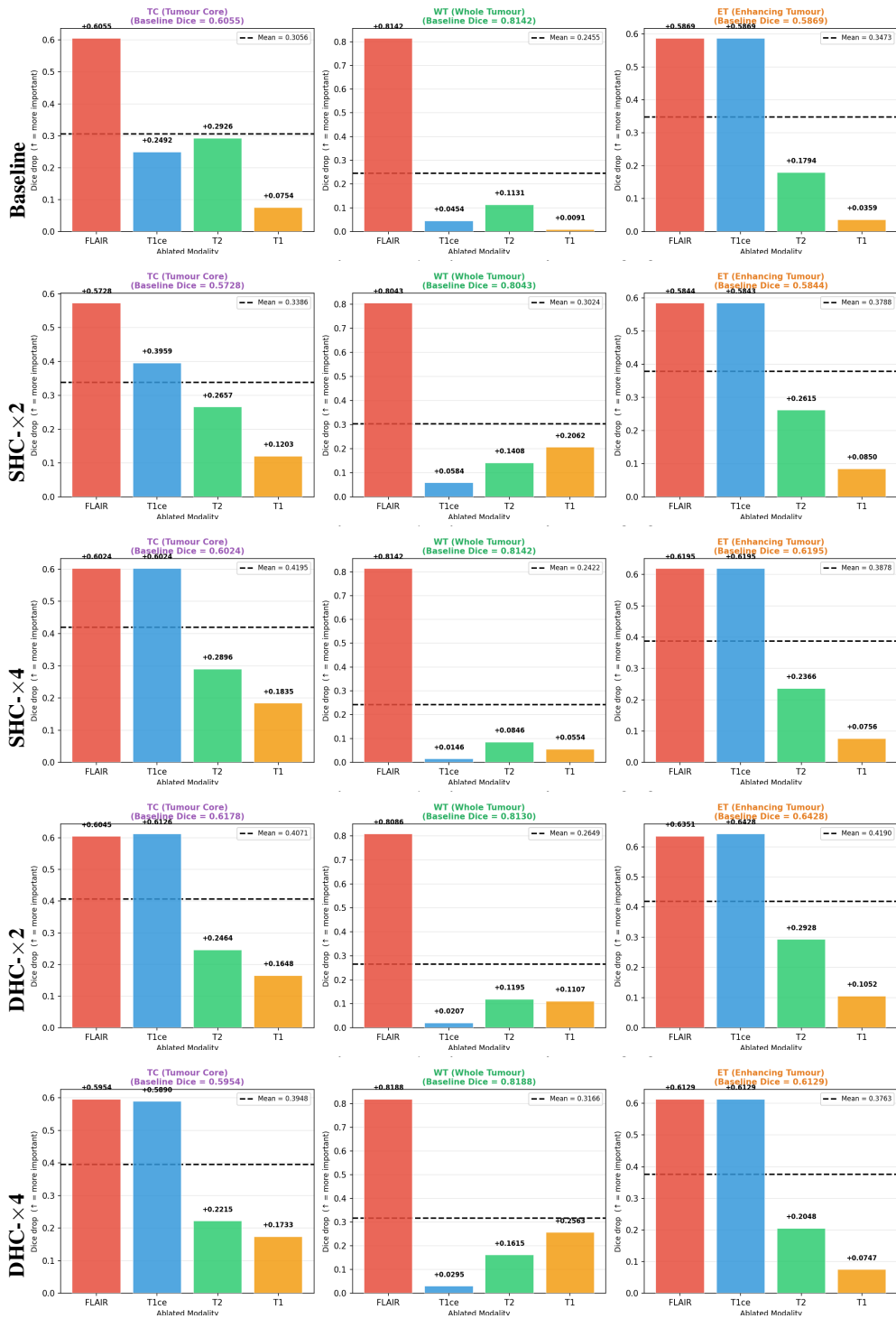


Figure 6: Modality ablation under different connection mechanisms (UNet).



Figure 7: Modality ablation under different connection mechanisms (UNetpp).

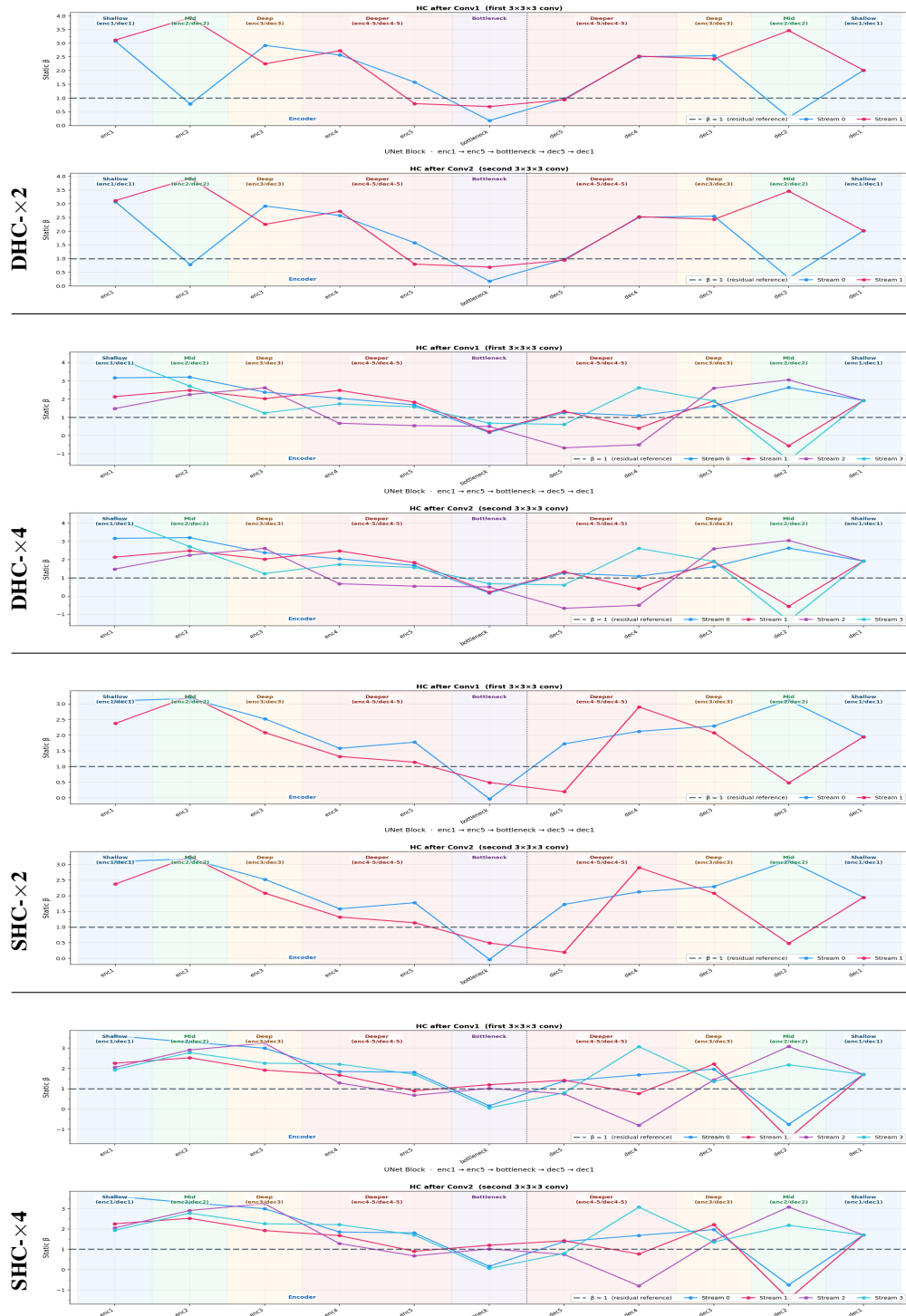


Figure 8: nnUNet3D β values across the model

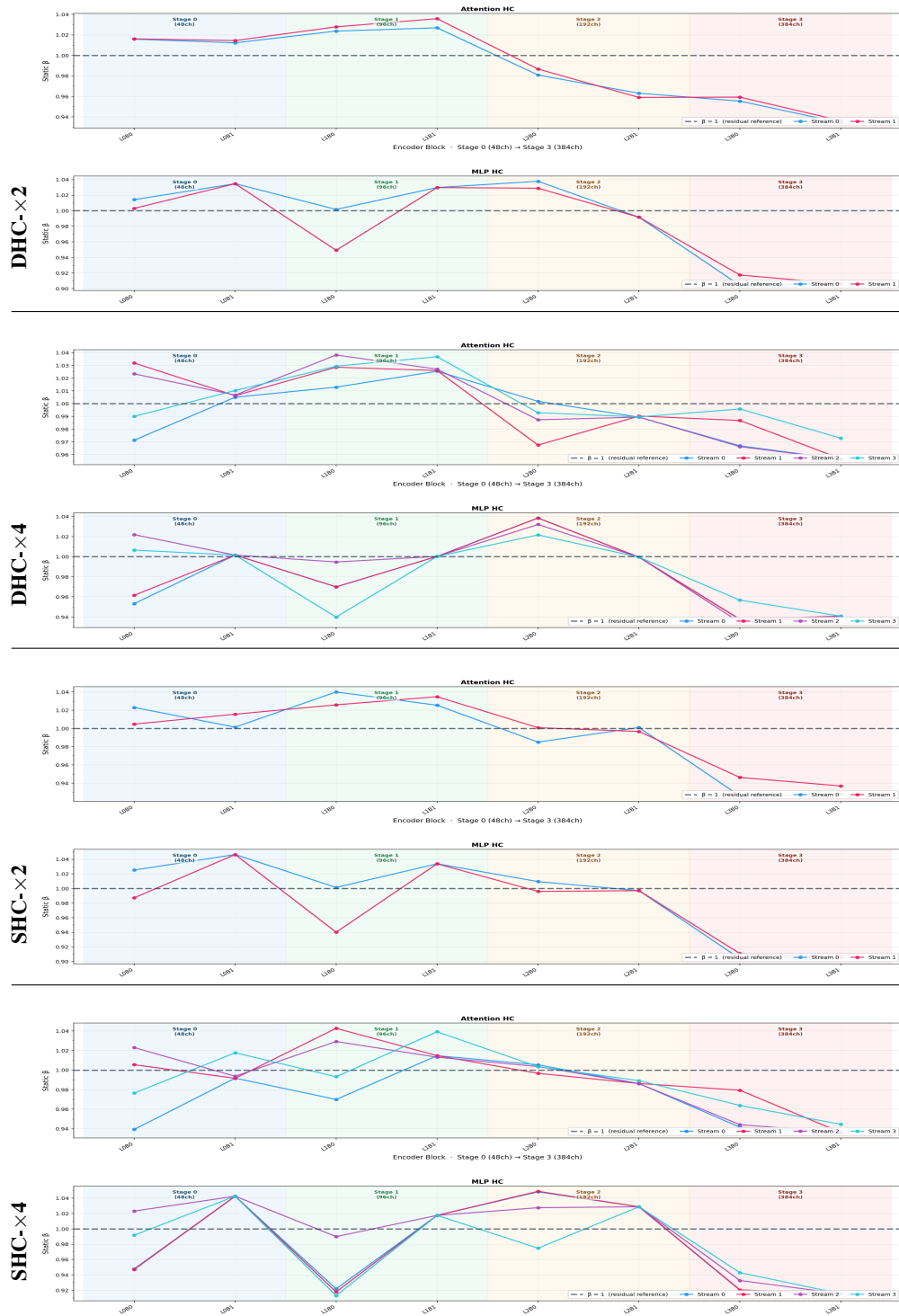


Figure 9: SwinUNETR3D β values across the model

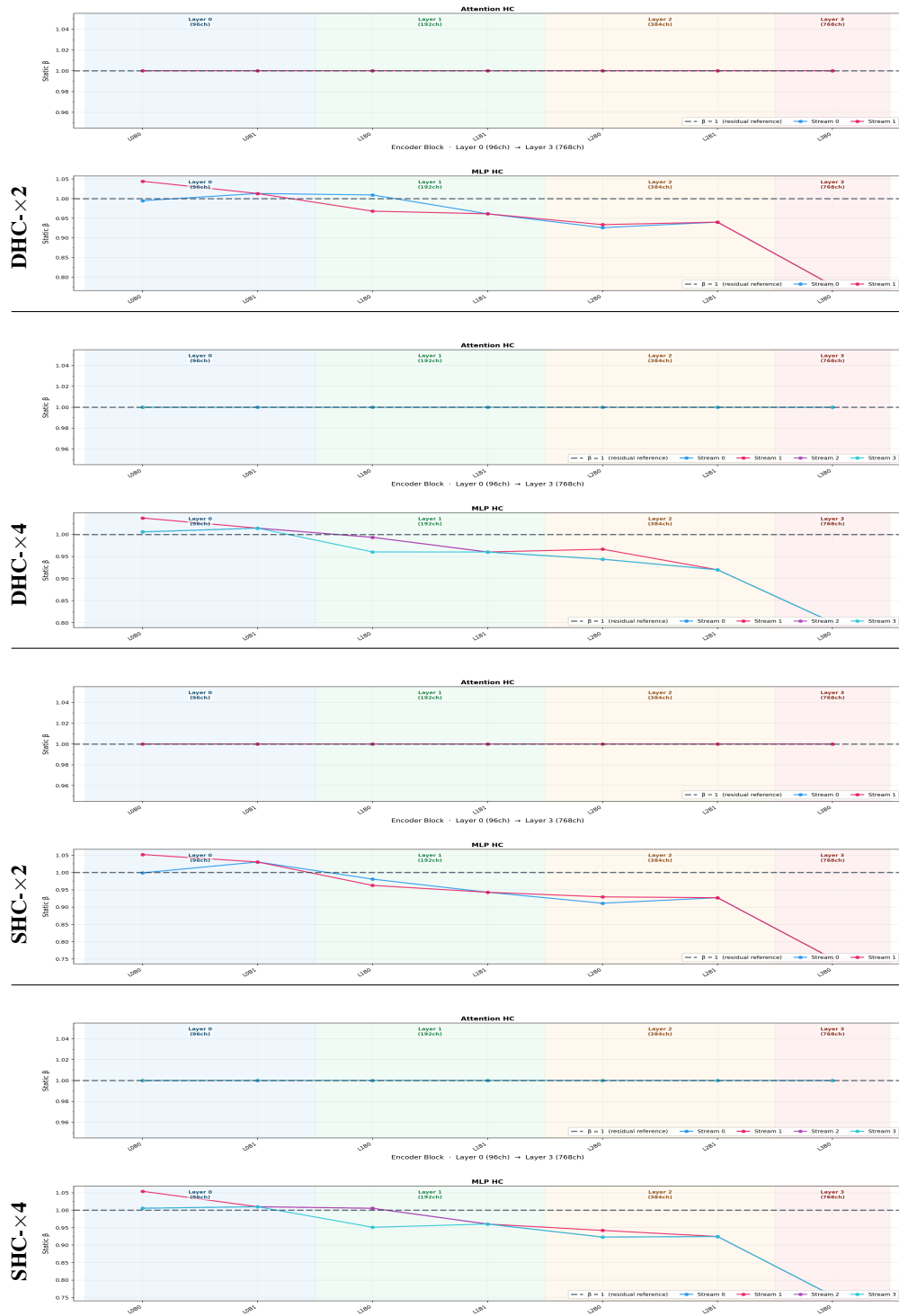


Figure 10: VTUNet3D β values across the model

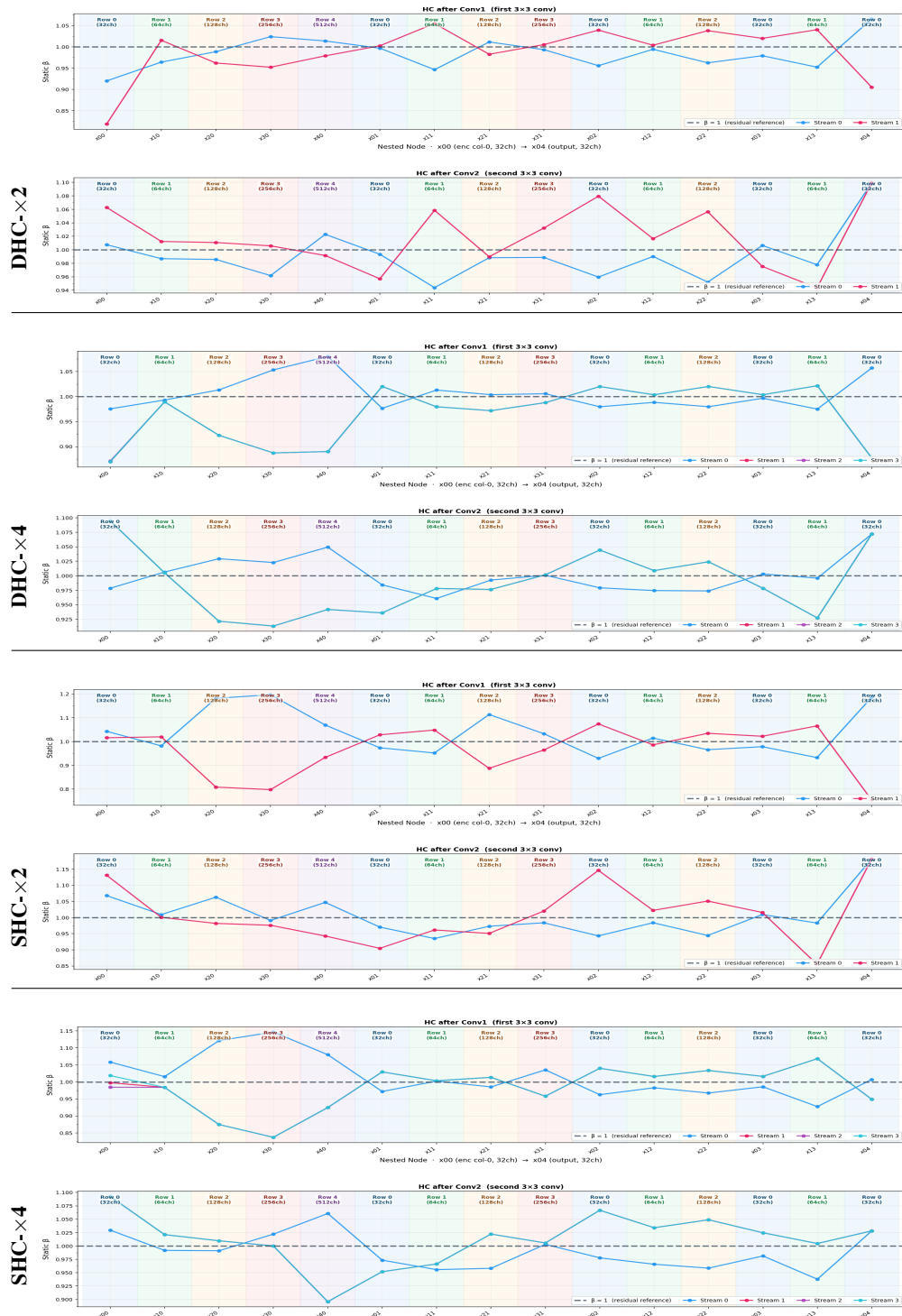


Figure 11: UNetpp2D β values across the model

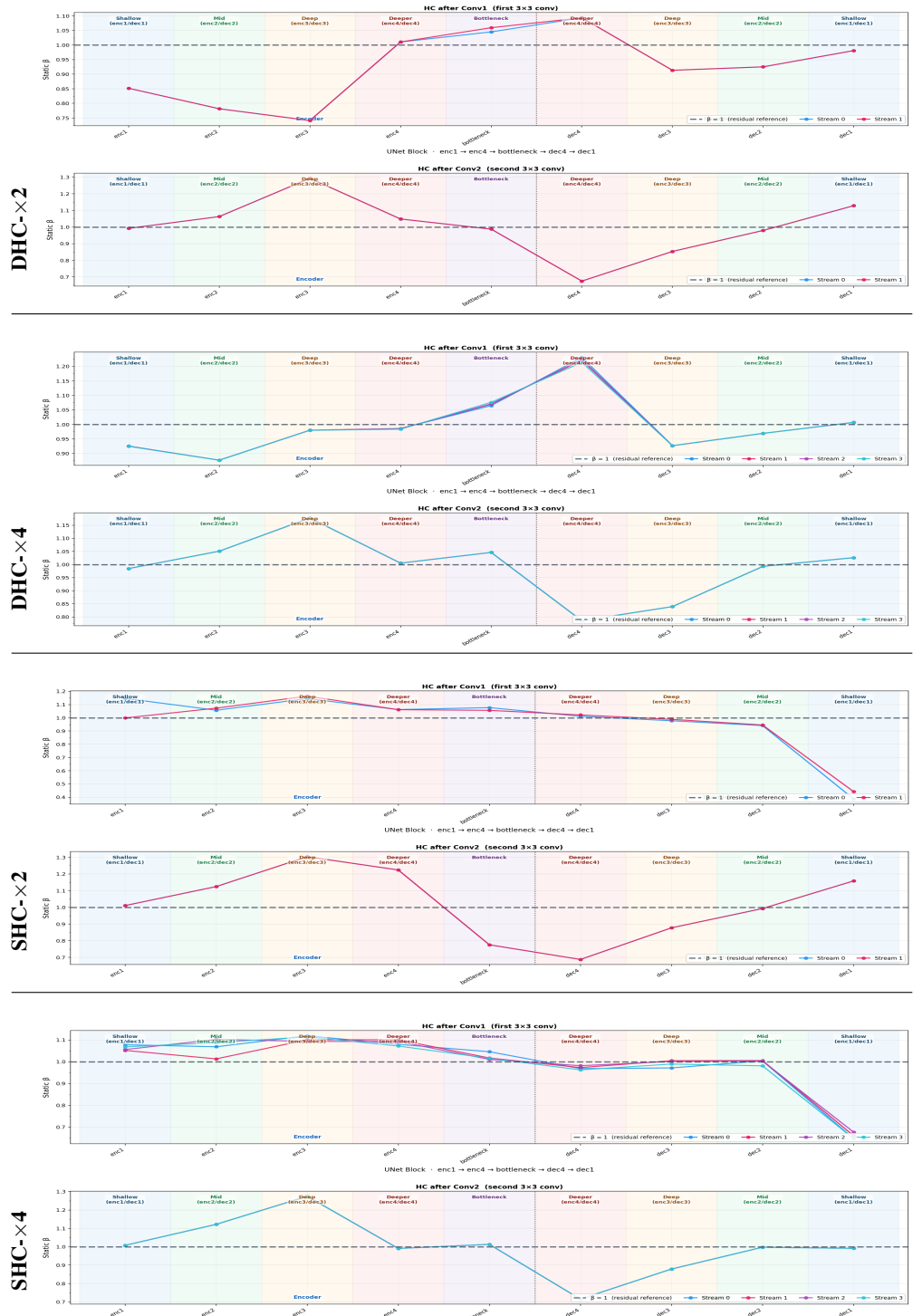


Figure 12: UNet2D β values across the model

| | TC | WT | ET | Dice TC / WT / ET / Mean |
|--------------|----|----|----|------------------------------------------------|
| Ground Truth | | | | |
| BaseLine | | | | TC 0.985 WT 0.981 ET 0.940 Mean 0.969 |
| DHC-x2 | | | | TC 0.986 WT 0.978 ET 0.956 Mean 0.973 |
| DHC-x4 | | | | TC 0.986 WT 0.981 ET 0.961 Mean 0.976 |
| SHC-x2 | | | | TC 0.987 WT 0.979 ET 0.958 Mean 0.975 |
| SHC-x4 | | | | TC 0.987 WT 0.978 ET 0.960 Mean 0.975 |

Figure 13: Qualitative results for nnU-Net. Rows correspond to Ground Truth, Baseline, DHC×2, DHC×4, SHC×2, and SHC×4. Columns correspond to TC (red), WT (blue), and ET (green). Dice scores for each configuration are shown on the right. HC-based models produce segmentations that more closely match ground truth boundaries, particularly for ET.

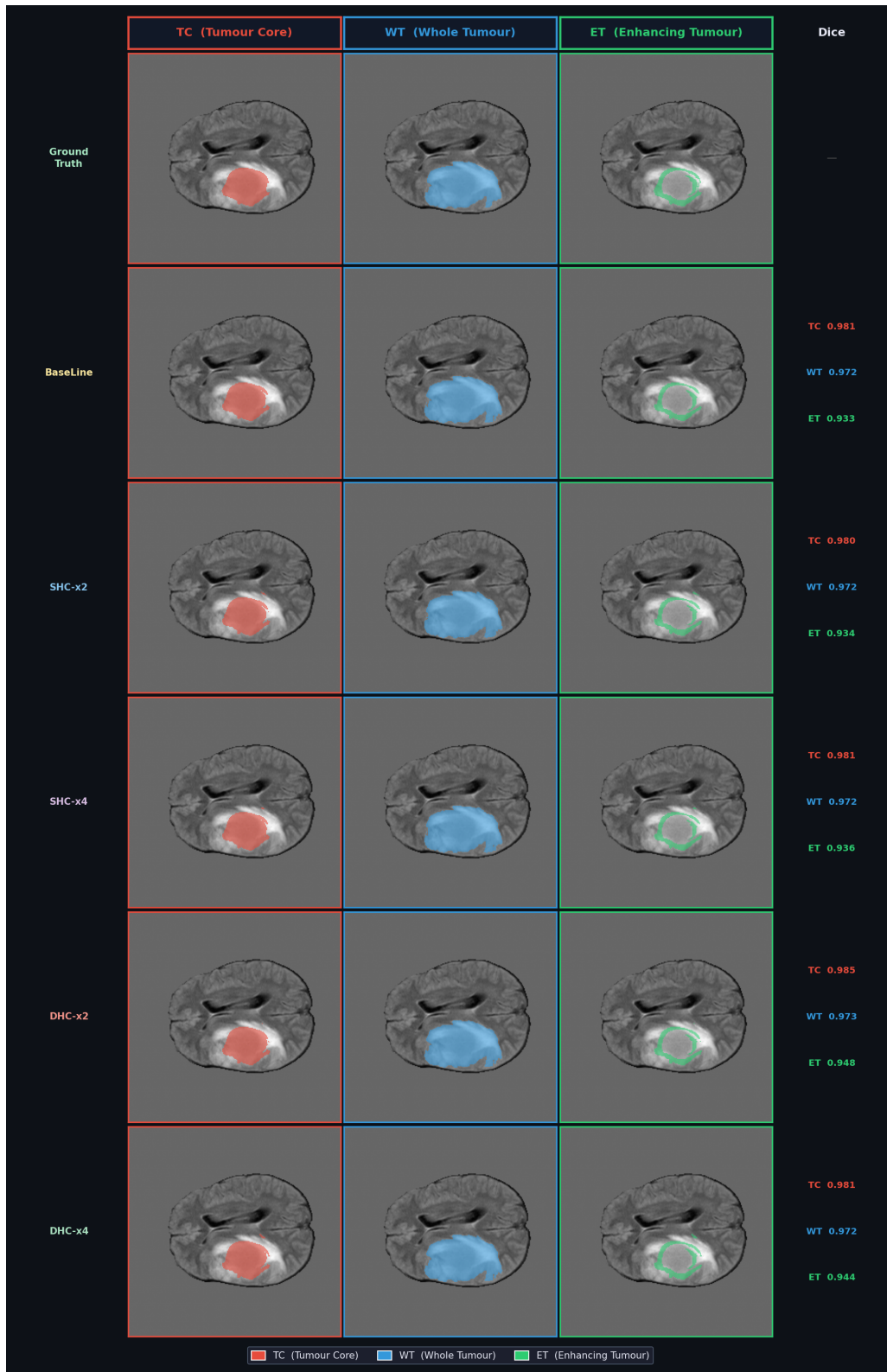


Figure 14: Qualitative results for SwinUNETR

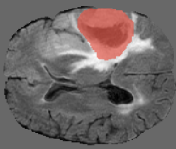
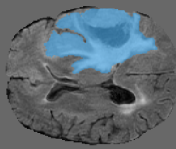
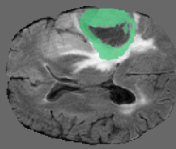
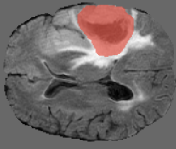
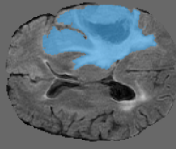
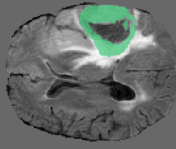
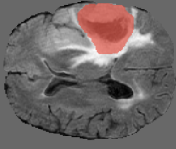
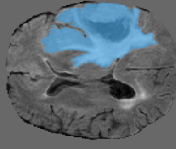
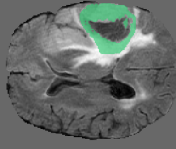
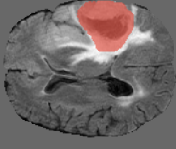
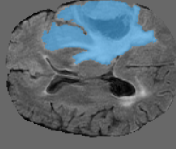
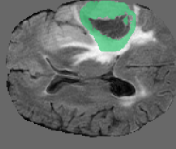
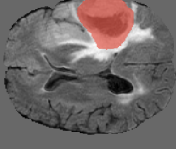
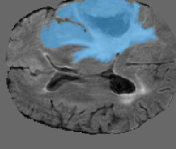
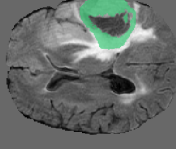
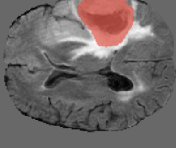
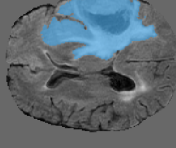
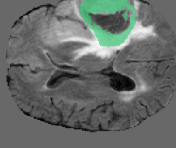
| | TC (Tumour Core) | WT (Whole Tumour) | ET (Enhancing Tumour) | Dice TC / WT / ET / Mean |
|--------------|-------------------------------------------------------------------------------------|-------------------------------------------------------------------------------------|--------------------------------------------------------------------------------------|------------------------------------------------|
| Ground Truth |  |  |  | - |
| BaseLine |  |  |  | TC 0.970 WT 0.952 ET 0.943 Mean 0.955 |
| DHC-x2 |  |  |  | TC 0.967 WT 0.949 ET 0.940 Mean 0.952 |
| DHC-x4 |  |  |  | TC 0.969 WT 0.948 ET 0.944 Mean 0.954 |
| SHC-x2 |  |  |  | TC 0.969 WT 0.942 ET 0.945 Mean 0.952 |
| SHC-x4 |  |  |  | TC 0.968 WT 0.945 ET 0.941 Mean 0.951 |

Figure 15: Qualitative results for VT-UNet

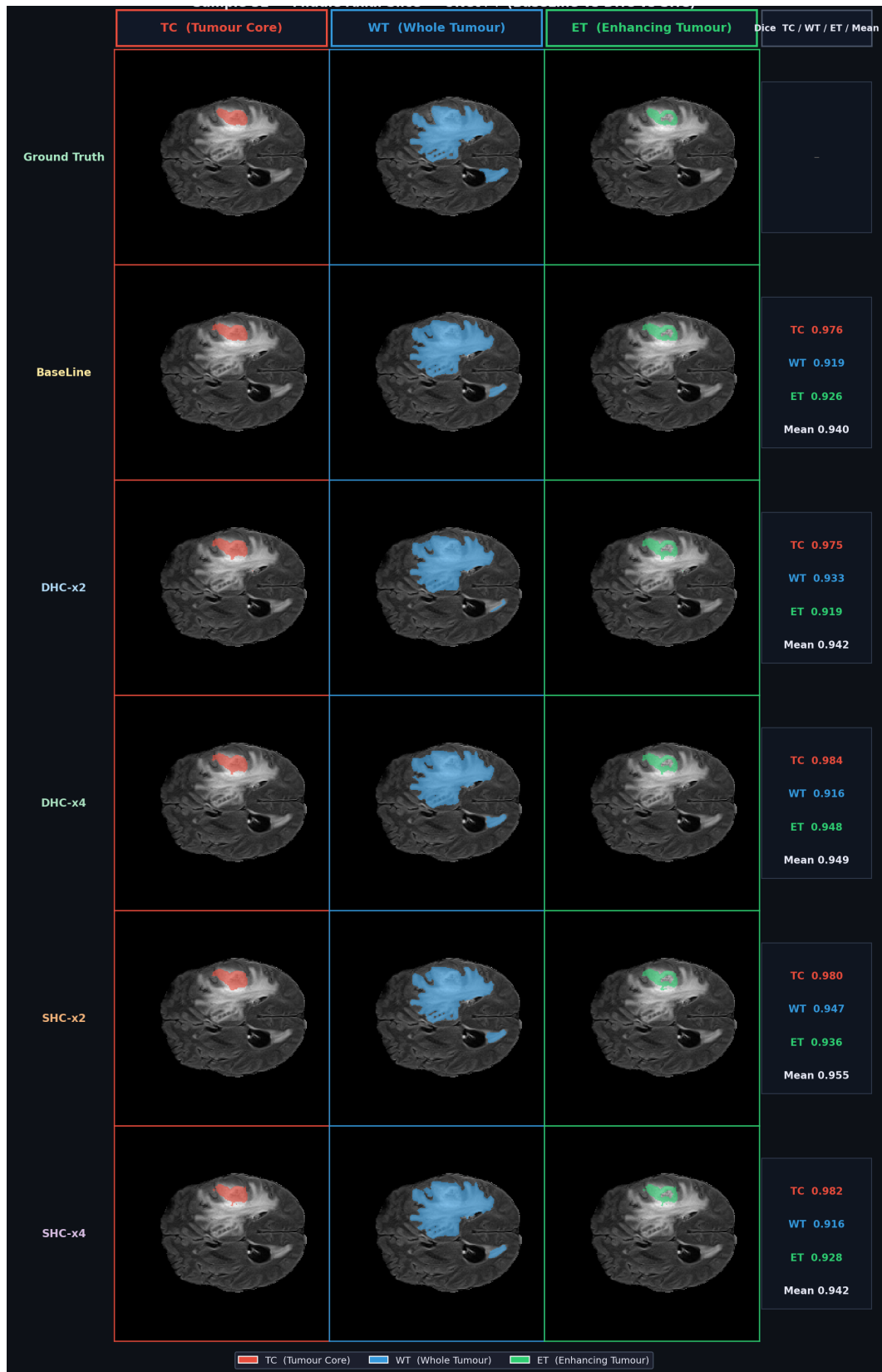


Figure 16: Qualitative results for U-Netpp

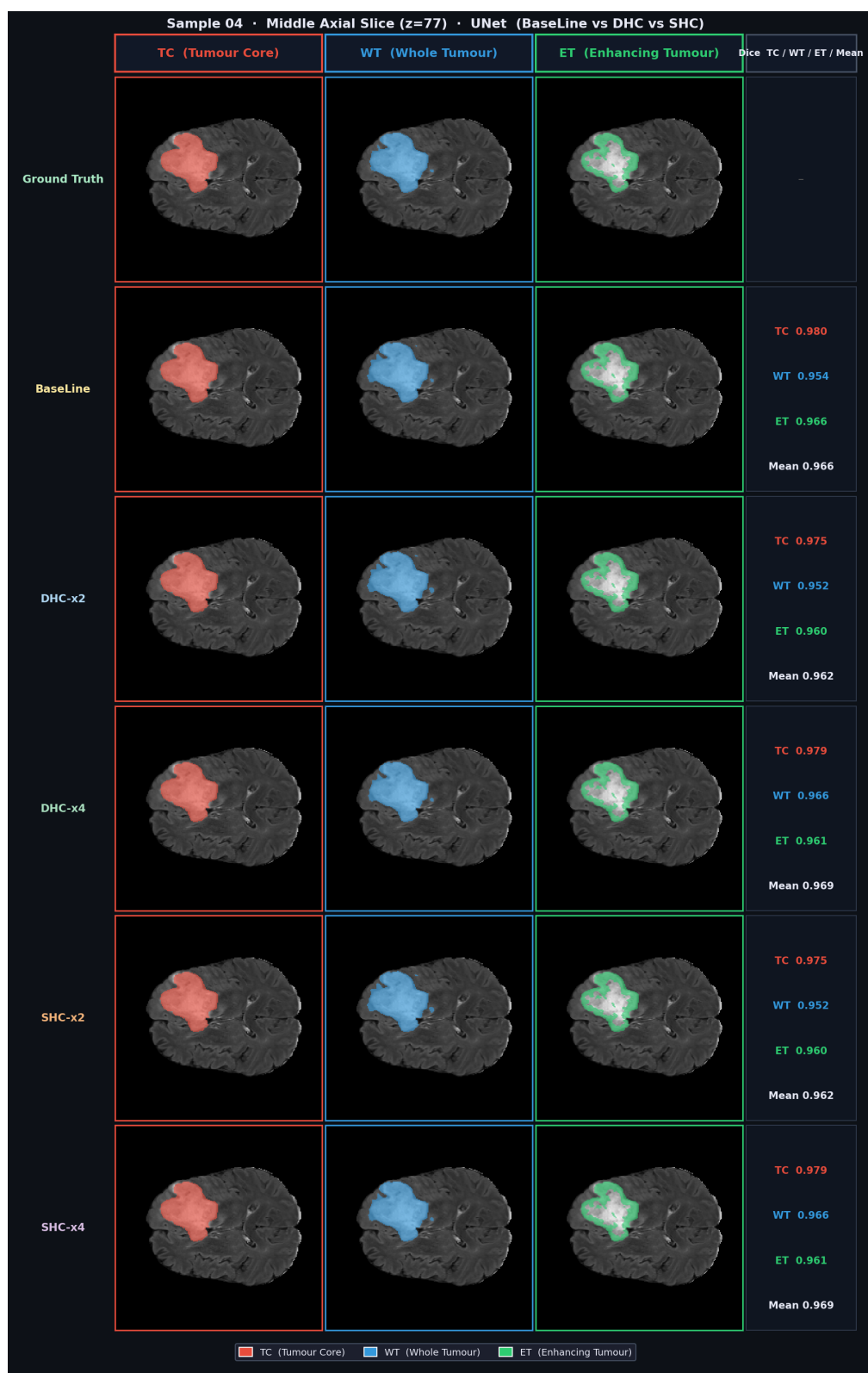


Figure 17: Qualitative results for U-Net